Measurement and models of bent KAP(001) crystal integrated reflectivity and resolution[a)]

G. P. Loisel,[1,b)] M. Wu[1], W. Stolte[2], C. Kruschwitz[3], P. Lake[1], G. S. Dunham[1], J. E. Bailey[1], G. A. Rochau[1]

[1]*Sandia National Laboratories, Albuquerque, New Mexico 87185, USA*
[2]*National Security Technologies, LLC, Livermore, California 94551, USA*
[3]*National Security Technologies, LLC, Los Alamos, New Mexico 87544, USA*

(Presented XXXXX; received XXXXX; accepted XXXXX; published online XXXXX)
(Dates appearing above are provided by the Editorial Office)

The Advanced Light Source beamline-9.3.1 x-rays are used to calibrate the rocking curve of bent potassium acid phthalate (KAP) crystals in the 2.3-4.5 keV photon-energy range. Crystals are bent on a cylindrically convex substrate with a radius of curvature ranging from 2 to 9" and also including the flat case to observe the effect of bending on the KAP spectrometric properties. As the bending radius increases the crystal reflectivity converges to the mosaic crystal response. The XOP multi-lamellar model of bent crystals is used to model the rocking curve of these crystals and the calibration data confirm that a single model is adequate to reproduce simultaneously all measured integrated reflectivities and rocking-curve FWHM for multiple radii of curvature in both 1st and 2nd order of diffraction.

I. Introduction

Potassium acid phthalate (KAP) crystals are routinely fielded in crystal spectrometers at the Z Pulsed Power Facility[1,2,3] to record soft x-ray spectra produced by high-energy-density plasmas. Because of the large orthorhombic unit-cell dimensions (a = 6.46 Å, b = 9.60 Å, and c = 13.32 Å), the (001) lattice with a $2d$ = 26.63 Å spacing can efficiently diffract soft x-rays down to ~500 eV photon energy. KAP crystals can be bent with appreciable quality making it useful for measuring a large spectral range using the cylindrically convex TIXTL instrument on Z[4-7]. Recently the opacity of Fe was measured in the 950-1700 eV range where Mg K-shell and Fe L-shell transitions are observed[8]. In these experiments the instrumental spectral resolution was dominated by the width of the rocking curve of the bent KAP crystal used and was calibrated in-situ using a Manson Source[9]. Besides resolution, the absolute spectral response of the instrument is of interest. Even though a transmission measurement only requires the cross-calibration of the spectrometers measuring the unattenuated and attenuated spectra[10], the absolute spectrometer response can be used to quantify the backlighter source spectral radiance[11]. Furthermore, measurements of the absolute integrated reflectivity in both 1st and 2nd order provide the ability to estimate and remove the effect of 2nd-order contamination on the data recorded in 1st order.

Up to now, Henke tables[12] were used to correct the data for instrument efficiency due to the lack of data for bent crystals, even though published Henke curves were obtained for flat crystals. Recent efforts established techniques to measure spectrometric properties of bent KAP crystals (i.e., integrated reflectivity and spectral resolution)[13,14]. The goal of the present study is to obtain calibration data for the actual crystal specimens used on Z and also to establish a predictive capability of the KAP crystal performance.

We used the x-rays from the Advanced Light Source (ALS) and recorded rocking curves in 1st and 2nd orders for the five 2", 4", 6", 9" and flat crystal curvatures. 180 rocking curves were collected and the data are compiled here. A single rocking-curve model for cylindrically bent crystals was adequate to interpret the entire dataset in the 2.3-4.5 keV photon-energy range.

II. Experimental setup

The experimental setup shown in Fig. 1 consists of a θ:2θ goniometer to measure the rocking curve of the crystal sample where the fixed x-ray source is the 9.3.1 ALS x-ray beamline. The x-ray beam operates in the 2.3-5.1 keV photon-energy range and is monochromated with two Si(111) crystals giving a resolving power of 3500-7000, depending on the energy. After the double-monochromator, the beam is sent to a toroidal Ni-coated mirror that focuses the beam in the goniometer chamber with 4-mrad and 0.5-mrad divergences in the horizontal and vertical dimensions, respectively. The beam was further collimated with a 5-μm pinhole to select the central bright and uniform part of the beam intensity profile. The Ni mirror also provides a hard x-ray cut-off at 5.3 keV such that higher-energy photons are effectively reduced avoiding measurement contamination. Each rocking curve is obtained by rocking the crystal about the Bragg angle, θ_B, satisfying the Bragg condition at the beamline energy, E, through 12.398/E [keV] = $2d$[Å]*sinθ_B and by rotating the detector by $2\theta_B$ to collect the total number of photons reflected off the crystal. The crystal θ-goniometer and the detector 2θ-goniometer have 0.017-mrad and 0.087-mrad angular resolution, respectively. Given that the smallest rocking-

[a)]Invited paper published as part of the Proceedings of the 21st Topical Conference on High-Temperature Plasma Diagnostics (HTPD 2016) in Madison, Wisconsin, USA.
[b)]Author to whom correspondence should be addressed: gploise@sandia.gov

curve width observed was about 0.08 mrad, the two goniometers have adequate angular resolution for the measurements presented here. The detector used is the Amptek XR-100SDD[15] multi channel analyzer (MCA) counting single photons that are incoming within 1 μs. This energy-dispersive detector allows us to integrate photon counts at the specific beamline energy. When two photons are counted simultaneously as a single event, a peak at twice the energy is observed. We monitored this peak and made sure that its intensity was kept below 1% of the beam energy peak by reducing the incident flux on the MCA.

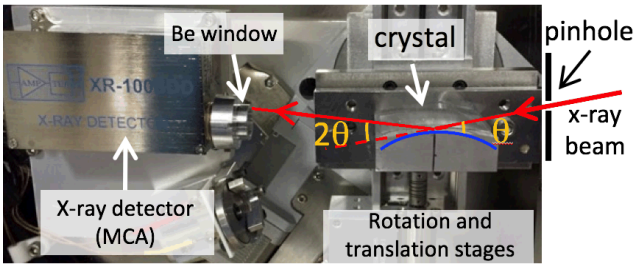

Figure 1: Rocking-curve θ:2θ goniometer at ALS 9.3.1 beamline. The pinhole on the right limits the beam size before it reaches the crystal and selects only the bright central part of the beam intensity spatial distribution. The bent crystals have a length of about 5 cm. A beryllium window keeps the detector light tight.

III. Rocking-curve measurement requirements

For the comparison with models, the rocking curves are reduced into two quantities: integral or integrated reflectivity, R_{int}, and full-width-at-half-maximum (FWHM). The integrated reflectivity does not depend on the shape of the rocking curve such that using different beam sizes or intrinsic source spectral widths from different techniques give similar R_{int} measurements[9,13]. For measuring R_{int} the first requirement is to have a high enough signal-to-noise ratio for increased calibration accuracy. This is easily obtained by increasing the duration of photon integration by the detector. The second practical requirement is a relatively fast data collection so multiple crystal specimens and multiple energies and multiple locations on the crystal surface can be obtained in a timely fashion with high signal-to-noise ratio. The total photon flux was limited by the ALS two-electron-bunch mode to 10^{10} photons/s. This photon flux is high enough to measure a single rocking curve in about 3 minutes with a signal-to-noise ratio of ~30 in 1st-order diffraction, so meeting our requirements for R_{int}.

Both crystal rocking-curve shape and width shall be used whenever evaluating the crystal-based instrument spectral resolution response. For instance, departures from trivial Gaussian or Lorentzian shapes can have a significant impact on the spectral resolution estimation[9]. Measuring the rocking-curve shape and width requires taking care of extra broadenings inherent to the calibration setup. In Ref. 9, this broadening was the intrinsic source line width from the Manson Source-produced characteristic lines. With the present synchrotron setup, the extra rocking-curve broadening can come from three contributions: i) the intrinsic beam spectral distribution, ii) the beam divergence independent of the crystal, and iii) the extra beam divergence after bouncing off the bent crystal surface. The intrinsic beam spectral distribution can be neglected here as it is equivalent to $\Delta\theta = \Delta E/E \tan\theta_B \sim 0.02$ mrad, significantly lower than any observed width. Fig. 2 b) and c) sketches show how contributions ii) and iii) broaden the measured rocking curve, respectively, in comparison to the ideal crystal-only case (Fig. 2a)). In general, these broadenings do not add their widths in quadrature since formally they are convolved together and their detailed profiles are usually not Gaussian.

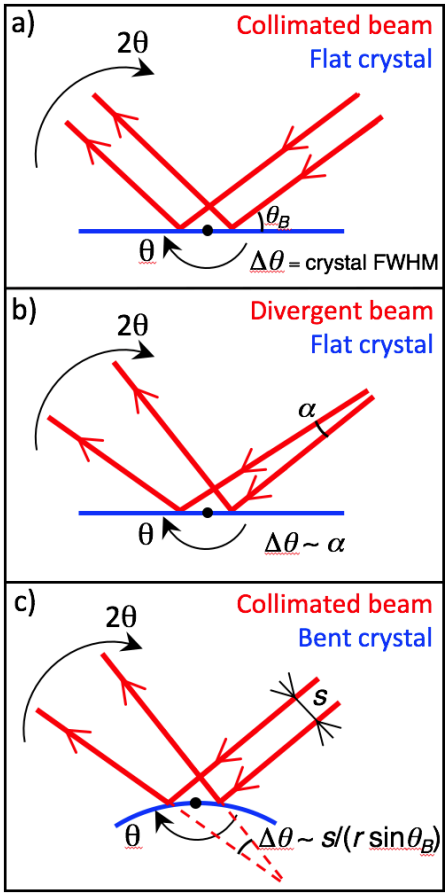

Figure 2: Contributions to the measured rocking curve. a) Collimated beam and flat crystal; the measured rocking curve is the crystal-only rocking curve. b) Divergent beam and flat crystal; the crystal rocking curve is broadened by the incident beam divergence. c) Collimated beam and bent crystal; the crystal rocking curve is broadened by the divergence induced by the crystal bending.

IV. Results and comparison with XOP

All measured rocking curves were best fit with a Voigt profile and reduced by taking the Voigt-fit integral as R_{int} and the Voigt-fit width as the rocking-curve FWHM. These rocking-curve moments were compared to the XCRYSTAL_BENT multi-lamellar bent-crystal-model part of the X-ray Oriented Programs (XOP)[16]. By default, the XOP bent-crystal program is run from a graphical interface, and a single rocking curve at a given energy is calculated. The XOP bent-crystal program has been modified to provide the inline calculation of the spectral R_{int} and FWHM for an arbitrary array of photon energies. The XOP rocking-curve model solves the Zachariasen formulation[17] for the dynamical theory of diffraction for ideally perfect plane crystals. The crystal

bending effects are treated using a multi-lamellar model that discretizes the crystal thickness into several flat layers that are slightly tilted with respect to each other to mimic the displacement of lattices induced in the crystal bending[18]. The XOP model includes the temperature factor (TF) parameter that can account for the effective crystal reflectivity upon the vibration of the unit-cell atoms about their mean positions[19]. The motion of unit-cell atoms disorganizes the lattices and effectively reduces the crystal reflectivity and increases the FWHM. The lower the temperature factor, the more important the temperature effect is; TF=1.0 is the unaffected reflectivity. We have no a priori knowledge on the correct value to choose for the temperature factor so it is considered as a free parameter and varied to find a value that best reproduced the calibration data consistently for all photon energies and bending radii.

A. 1st-order integrated reflectivity

Fig. 3 compiles the results for the 1st-order integrated reflectivity for the five crystal curvatures studied. The error bars shown correspond to the individual measurement propagated error on the fit parameters. The scatter of data taken at nearby energies suggests that the true uncertainties are actually larger at the level of ~10%. The photon-energy range included the potassium-K edge at 3608 eV, which corresponds to a discontinuous reflectivity drop. Since for all plots the y-axis is set to show the same 0.0-0.23 mrad range, one can readily see the trend for R_{int} as the crystal is more bent, in particular for energies below the potassium-K edge. Larger bending corresponds to larger integrated reflectivity. The XOP R_{int} are calculated for the three 1.0-, 0.9-, and 0.8-temperature factors. The experimental data are well matched for a temperature factor between 0.8 and 0.9 for all the curvatures. In the flat-crystal case the data are superimposed with the Henke Darwin-Prins perfect-crystal and mosaic models[18]. One can see that the Henke perfect-crystal model is relatively close to the flat-crystal data with the exception of a ~100-eV offset in the predicted location of the potassium-edge feature. The Henke mosaic model shares similar spectral shape with the bent cases confirming the expectation that the effect of bending is somewhat comparable to an increase in crystal mosaicity. The data points and XOP R_{int} are converging to the Henke mosaic model at the 2" radius (see Fig. 2 bottom plot). For other radii, R_{int} is dependent on the exact level of bending and better represented by the XOP calculations than either perfect-crystal or mosaic models.

B. 2nd-order integrated reflectivity

Fig. 4 shows the integrated diffraction profile in 2nd order. The effect of the potassium-K edge is again visible but this time results in increased reflectivity compared to the 1st-order case. Even though the dataset is sparser due to the longer exposure time required, it is consistent with the K-edge structure. In Fig. 4 we compared data again with the XOP model in 2nd order for the same set of temperature factors. The dependence of reflectivity on the TF is less pronounced in second order compared to first order such that the data are compatible with a TF between 0.9 and 1.0. For reference, the Henke calculations are shown in the flat case. Similar inferences can be drawn here: the flat-crystal data agrees well with the perfect case and the flat-mosaic response goes in the direction of the bent reflectivity, still with a ~100-eV offset in the predicted edge-effect location.

C. Flat crystal 1st- and 2nd-order resolution

For the flat case, there is no geometrical broadening due to the reflection of the beam on a bent surface such that only the beam divergence is broadening the crystal rocking curve. Given that the observed width for the flat crystal is systematically larger than XOP or Henke predictions, we scrutinized the effect of the beam diffraction by the pinhole used to restrict the beam size. Fig. 5 shows that a relatively good agreement is obtained when the XOP rocking curve is convolved with the Fresnel-diffracted beam profile after the beam went through the pinhole. At first, we did not expect the diffraction to be important here since the ratio of pinhole size to photon wavelength is $5.0 / 0.00054 \sim 10^4$ and the pinhole to detector distance is 30 cm, but it turns out to be about a 50% contribution to the total width in 1st order and almost entirely dominating the 2nd-order width with ~80% contribution.

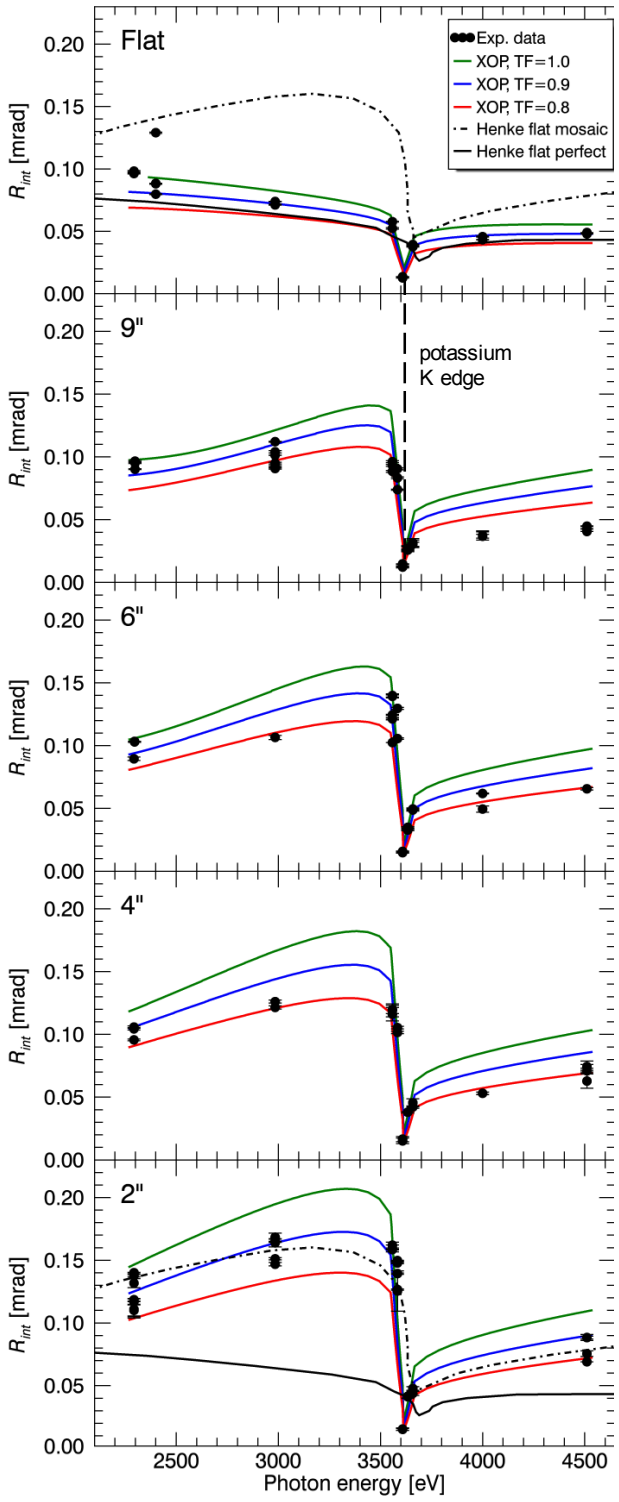

Figure 3: Integrated reflectivity in 1st order for the different radii of curvature as labelled in the upper left corner of each plot. The vertical axes span the same range illustrating the trends in the reflectivity as the curvature changes. The XOP calculations are overlaid for TF=1.0, 0.9, and 0.8. The flat and 2" cases include Henke perfect and mosaic models.

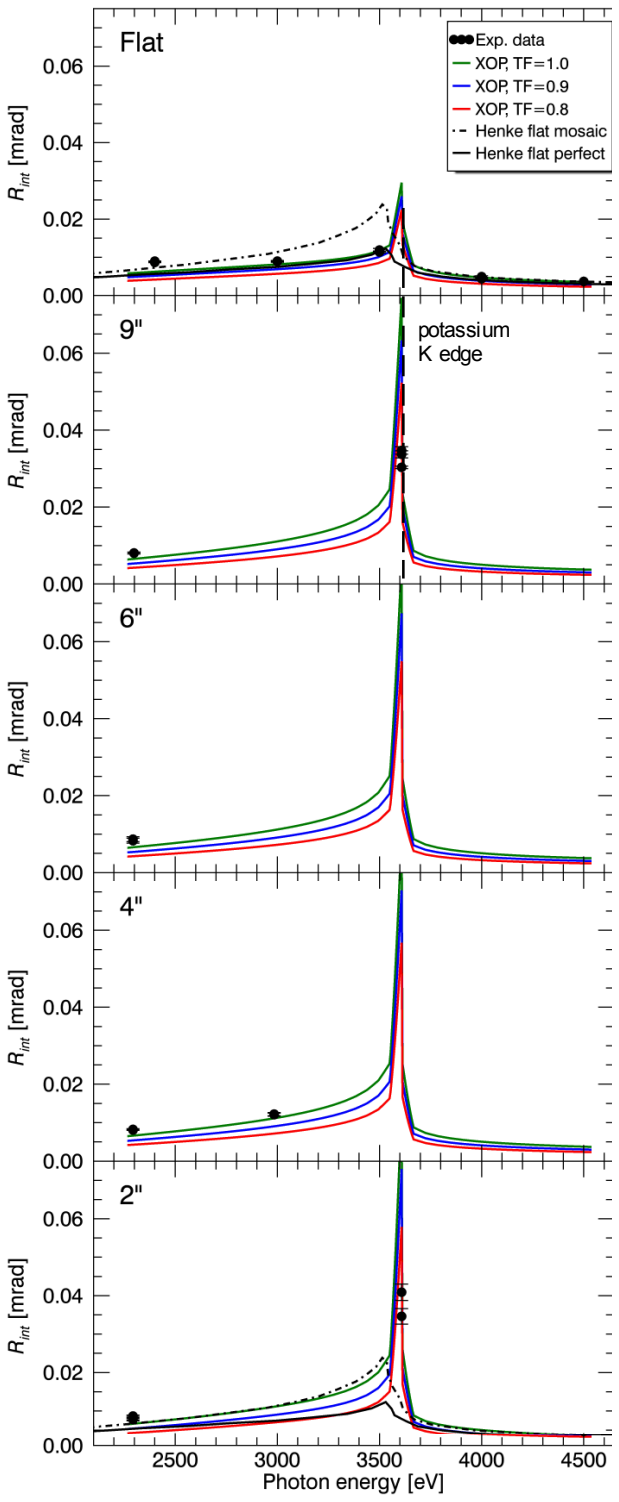

Figure 4: Integrated reflectivity in 2nd order for the different radii of curvature as labelled in the upper left corner of each plot. The vertical axes span the same range illustrating the trends in the reflectivity as the curvature changes. The XOP calculations are overlaid for TF=1.0, 0.9, and 0.8. The flat and 2" cases include Henke perfect and mosaic models.

In this situation we can in principle extract the intrinsic crystal rocking-curve width in 1st order by deconvolving the 2nd-order measurement from the 1st-order one. If we approximate the

diffracted beam profile by a Gaussian profile with an expected width of ~0.09 mrad (see Fig. 5 bottom at 2.5 keV) and the crystal rocking curve to a Lorentzian profile, then we can analytically estimate the crystal rocking-curve width from the deconvolution of the measured Voigt width of 0.15±0.01 mrad from the diffracted beam profile. We find a crystal Lorentzian width of 0.10±0.015 mrad similar to the XOP prediction. The reason to assume that the crystal rocking curve is Lorentzian comes from the fact that XOP predicts rocking curves that are asymmetric but almost Lorentzian for the photon-energy range studied here. The details of the exact profile deconvolution and a more accurate evaluation of the uncertainties will be addressed in a future publication.

The diffraction broadening in 2nd order is too large to reasonably get a 2nd-order crystal rocking curve with enough accuracy. We are not including here the results for the width for the bent crystals in 1st order since for those the beam reflection off the bent surface at relatively small angles (<11°) is significant and clearly dominates the observed widths.

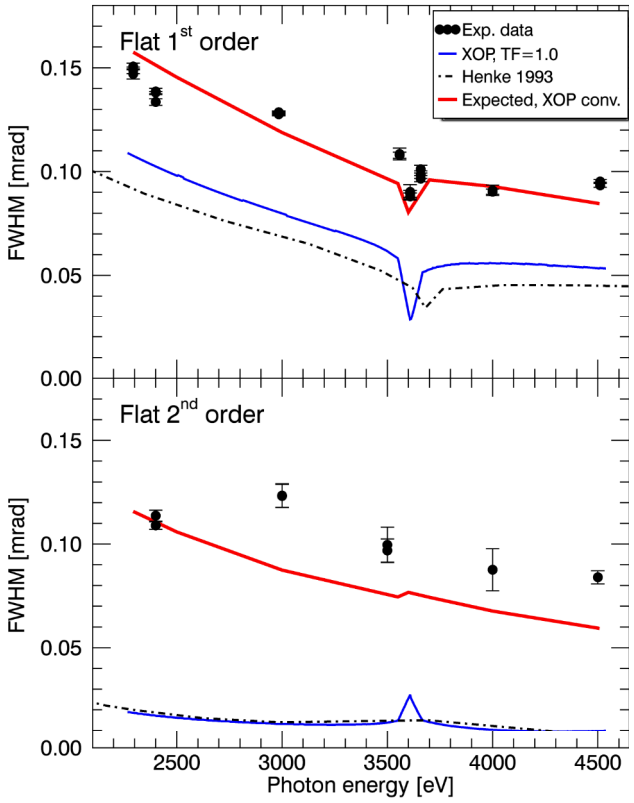

Figure 5: Rocking-curve FWHM for the flat crystal. Top: 1st-order case, the expected magenta curve corresponds to the XOP results convolved with the Fresnel-diffracted beam profile. Bottom: 2nd-order case, same legend. The Henke calculations[20] are overlaid.

D. Bent-crystal 2nd-order resolution

Fig. 6 shows that the measured 2nd-order widths for the bent crystals are at least twice as large as for the flat crystal. They are also larger than the diffraction contribution from the pinhole shown in Fig. 5.

As indicated in Fig. 2 c), the geometrical contribution from the crystal bending is given by the angle subtended by the projected beam size s on the crystal surface from the crystal center of curvature (i.e., $s/r*\sin\theta_B$ where r is the crystal radius. In 2nd order, the projected beam size on the crystal surface is reduced by a factor of 2 compared to 1st order at a given photon energy. Numerically, for the lowest 15.5° Bragg angle in the 2nd order and for the diffracted 7-µm beam size, this geometrical contribution from the crystal bending equals 0.08, 0.12, 0.18, and 0.36 mrad for the 9, 6, 4, and 2" radii respectively. Fig. 6 shows that the width measurements are significantly larger than these values suggesting that they are not dominating the observed widths. Therefore, the measurements should be dominated by the intrinsic crystal rocking-curve width for the bent crystals in 2nd order. The level of agreement with the XOP calculations confirms this result. This is the indication that the XOP multi-lamellar model for bent crystals is suitable to predict crystal resolution when the total rocking-curve width is dominated by the intrinsic crystal bending.

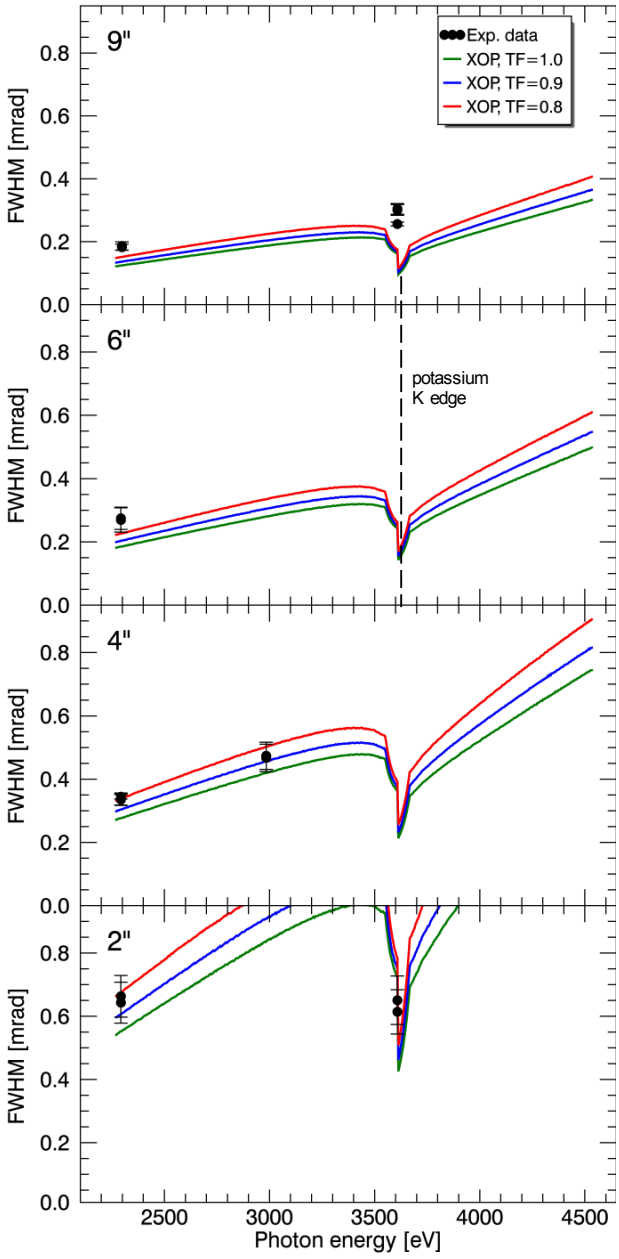

Figure 6: Rocking-curve FWHM in 2nd order for 9, 6, 4, and 2" radius of curvature as labelled in the upper left corner of each plot. The vertical axes span the same range illustrating the trends in the reflectivity as the curvature changes. The XOP calculations are overlaid for the 1.0, 0.9, and 0.8 temperature factors.

V. Discussion and future plans

The XOP calculations adjusted with the inferred temperature factors in the present study are used to unfold Z data taken with the convex-crystal TIXTL instrument. The success in reproducing the absolute integrated reflectivities makes us confident in the presented technique such that similar modeling and calibration efforts will be conducted for the lower 700-2000 eV photon-energy range where the opacity data have been collected on Z. This spectral energy range was not accessible to us at the ALS but a new beamline at the Stanford synchrotron SSRL will provide this range. Our resolution measurements are consistent with our model prediction including systematic broadening from the experimental apparatus. In the future, the detailed deconvolution analysis will be conducted to better evaluate resolution accuracy of the method. A first estimate led to a 15% accuracy in resolution when the beam divergence contributed to 50% of the observed rocking-curve width. Future plans include adapting the technique presented here to different crystals routinely used at the Z facility, such as cylindrically convex RbAP, spherically concave quartz, and elliptically bent crystals.

VI. Acknowledgments

We thank M. J. Haugh for his expertise and his assistance in collecting rocking-curve data. We thank M. Sánchez del Rio for reading and approving this work and the use of the XOP code. We thank Sandia National Laboratories is a multiprogram laboratory managed and operated by Sandia Corporation, a wholly owned subsidiary of Lockheed Martin Corporation, for the U.S. Department of Energy's National Nuclear Security Administration under Contract No. DE-AC04- 94AL85000.

VII. References

[1]D. H. McDaniel, M. G. Mazarakis, D. E. Bliss, et al., in AIP Conf. Proc. 651, 5th Int. Conf. on Dense Z-Pinches, ed. J. Davis, C. Deeney & N. R. Pereira, **23** (2002).
[2]M. K. Matzen, Sweeney M. A., R. G. Adams et al., 2005, Phys. Plasmas, **12**, 055503, (2005).
[3]M. E. Savage, K. R. LeChien, M. R. Lopez et al., in 18th IEEE Pulsed Power Conf. (PPC), **983**, (2011).
[4]M. deBroglie and F. A. Lindemann, C. R. Acad. Sci. Paris, **158**, 944 (1914).
[5]L. S. Birks, Rev. Sci. Instrum., **8**, 1129, (1970).
[6]N. J. Peacock, R. J. Speer and M. G. Hobby, J. Phys. B, **2**, 798 (1969).
[7]T. J. Nash, et al., Rev. Sci. Instrum., 72, 1167, (2001)
[8]J.E. Bailey, T. Nagayama, G. P. Loisel et al., Nature, **517**, 56, (2015).
[9]G. Loisel, J. E. Bailey, G. A. Rochau, G. S. Dunham, L. B. Nielsen-Weber and C. R. Ball, Rev. Sci. Instrum. **83** 10E133 (2012).
[10]J. E. Bailey, G. A. Rochau, R. C. Mancini, C. A. Iglesias, J. J. MacFarlane, I. E. Golovkin, C. Blancard, Ph. Cossé and G. Faussurier, Phys. Plasmas, **16**, 058101 (2009).
[11]T. Nagayama, J. E. Bailey, G. Loisel, G. A. Rochau, J. J. MacFarlane, and I. Golovkin, Phys. Rev. E, **93**, 023202 (2016).
[12]B. L. Henke, E. M. Gullikson & J. C. Davis. *Atomic Data and Nuclear Data Tables*, **54**(2), 181(1993).
[13]M. J. Haugh, M. Wu, K. D. Jacoby and G. P. Loisel, Rev. Sci. Instrum., **85**,11D619 (2014).
[14]M. J. Haugh, J. J. Lee, K. D. Jacoby, C. Christensen and G. Loisel, Proc. of SPIE, **9591**(2015).
[15]http://amptek.com/products/xr-100sdd-silicon-drift-detector/
[16]M. Sánchez del Río and R. J. Dejus, SPIE proceedings, **8141**, 814115 (2011). http://www.esrf.eu/Instrumentation/software/data-analysis/xop2.4
[17]W. Zachariasen, Theory of x-ray diffraction in crystals. New York:Dover, (1967).
[18]M. Sánchez del Río et al., J. Appl. Crystallogr., **48**(2), 477, (2015).
[19]B. D. Cullity, Elements of X-ray Diffraction, 2nd Edition. Addison-Wesley Publishing Company Inc.
[20]B. L. Henke, Technical Notes on High Energy X-Ray Response of Some Useful Crystal Analyzers, Sandia located Henke Notes compilation, 1987.